MATERIALS ENGINEERING

Biomimetic nanocoatings with exceptional mechanical, barrier, and flame-retardant properties from large-scale one-step coassembly

Fuchuan Ding,[1,2]* Jingjing Liu,[1]* Songshan Zeng,[1] Yan Xia,[1] Kacie M. Wells,[1] Mu-Ping Nieh,[1] Luyi Sun[1,2]†

Large-scale biomimetic organic/inorganic hybrid nanocoatings with a nacre-like microstructure were prepared via a facile coassembly process. Different from conventional polymer nanocomposites, these nanocoatings contain a high concentration of nanosheets, which can be well aligned along the substrate surface. Moreover, the nanosheets and polymer matrix can be chemically co–cross-linked. As a result, the nanocoatings exhibit exceptional mechanical properties (high stiffness and strength), barrier properties (to both oxygen and water vapor), and flame retardancy, but they are also highly transparent (maintaining more than 85% of their original transmittance to visible light). The nanocoatings can be applied to various substrates and regular or irregular surfaces (for example, films and foams). Because of their excellent performance and high versatility, these nanocoatings are expected to find widespread application.

INTRODUCTION

Through millions of years of evolution, many biological systems have developed to realize virtually perfect unification of their structures and thus optimized properties. They are usually made of organic and inorganic components arranged in a complicated but amazingly hierarchical structure, enabling them to have a unique combination of remarkable stiffness, strength, toughness, low density, and possibly extra functionality (*1*, *2*). One of the most outstanding and representative examples is nacre.

Nacre is an organic/inorganic composite with outstanding strength, stiffness, and toughness (*2*–*6*). Nacre is composed of ca. 95 volume percent (volume %) of inorganic calcium carbonate (in the form of aragonite) and ca. 5 volume % of organic biopolymers (β-chitin and silk fibroin proteins), both having ordinary mechanical properties (*7*, *8*). The striking contrast between the exceptional mechanical properties of nacre and their ordinary components has inspired materials scientists to synthesize organic/inorganic hybrids with a similar structure for practical applications. The key structural features of nacre are a high concentration of well-aligned nanosheets (fig. S1) and a strong interface. Nature has adopted an elaborate strategy to create nacre (*9*–*13*), involving a multistep biomineralization process (*14*). Although this process has been mimicked in vitro (*11*, *15*), it is very difficult to scale up this highly delicate biological process. In addition to mineralization (*16*, *17*), a number of approaches, including ice-templated synthesis (*6*, *18*), layer-by-layer (LbL) self-assembly (*19*–*22*), and electrophoretic deposition (*23*), have been explored to form a nacre-like microstructure. Although each of the above approaches has its own advantages, it remains a huge challenge to achieve large-scale continuous mass production of large-sized samples.

It is well known and intuitively understandable that flow can help induce orientation (*24*–*26*). However, concentrated suspensions of fillers can pose difficulties in achieving filler alignment (*24*). Here, we design to create a low-viscosity liquid flow containing both inorganic nanosheets and polymer binders, to help align nanosheets on a substrate surface along the flow direction. During the flow-induced orientation, the nanosheets and polymer chains are expected to coassemble to form a highly ordered layered structure with dozens of layers within a single step, whereas the ratio of the nanosheets and polymer can be easily adjusted, both of which make this process distinctively different from and easier than the LbL assembly (*21*).

RESULTS

Coassembled nanostructured hybrid nanocoatings and structural characterization

Montmorillonite (MMT) can exfoliate into individual single-layer nanosheets with a thickness of ca. 1.0 nm (*27*) in aqueous system with the assistance of ultrasonication (*22*). The transmission electron microscopy (TEM) image and lateral dimension distribution (260 ± 60 nm) of the exfoliated MMT nanosheets are shown in fig. S2. Meanwhile, polyvinyl alcohol (PVA) was dissolved in water to form a solution. Then, the two components were mixed at predetermined ratios. Extra water can be added to adjust the overall concentration. Because of the weak interactions, mainly hydrogen bonding and van der Waals interactions (*22*), between the MMT nanosheets and the PVA chains, the PVA chains can attach to the MMT nanosheet surface (Fig. 1) (*22*, *28*, *29*), which is critical for the following coassembly process. The dispersion was coated on polylactic acid (PLA) films (or other substrates) through a very simple dip-coating process, and the films were subsequently hung vertically so that the MMT nanosheets can be aligned with the assistance of the flow of a thin layer of liquid (Fig. 1) induced by the gravity. A dispersion of 1.5 weight % (wt %) of solids (MMT + PVA) was chosen to ensure a low viscosity to create a quick flow and a thin liquid layer, both of which are highly desirable to achieve a high level of orientation of nanosheets (*30*). The coated PLA films were dried at 60°C in an oven, during which PVA was dried and sandwiched between well-aligned MMT nanosheets. The coated samples were labeled as PLA (or other polymer)–PVA/MMT-*X*-C (or N), where *X* is the mass percentage of MMT in the mixture of MMT and PVA in the initial formulation; C refers to "cross-linked," and N refers to non–cross-linked.

[1]Department of Chemical and Biomolecular Engineering and Polymer Program, Institute of Materials Science, University of Connecticut, Storrs, CT 06269, USA. [2]Department of Chemistry and Biochemistry, Texas State University, San Marcos, TX, 78666, USA.
*These authors contributed equally to this work.
†Corresponding author. Email: luyi.sun@uconn.edu

The coated PLA films exhibited very high transparency even when the nanocoating contains up to 70 wt % of MMT nanosheets (Fig. 2A), indicating that a high level of dispersion and orientation of MMT nanosheets was achieved in the nanocoating. Moreover, the ultraviolet-visible (UV-Vis) spectra also exhibited the Fabry-Pérot patterns, further suggesting high uniformity in the nanocoating (*22*, *31*). This result is highly in contrast to the conventional nanocomposites, which typically cannot maintain high transparency when the nanofiller loading is above ca. 10 wt % (*32*, *33*).

The level of MMT nanosheet orientation is the most critical factor to the quality of the formed nanocoating, which was systematically characterized by x-ray diffraction (XRD), TEM, and small-angle x-ray scattering (SAXS). The intense basal diffraction peaks shown in the XRD patterns (Fig. 2B) support the idea that the MMT nanosheets were well oriented, especially the ones containing 30 wt % of MMT or higher. The patterns show an apparent trend. With an increasing concentration of MMT nanosheets in the nanocoating, their interlayer distance decreased, which was simply due to the reduced amount of PVA chains within the MMT layers. Note that the PVA/MMT-20-C sample exhibited the broadest peak, whereas the PVA/MMT-50-C nanocoating exhibited the narrowest peak. The above results suggest that, when MMT nanosheet concentration was too low, it was not beneficial for orientation, which was probably because there was sufficient space for MMT nanosheets to rotate during/after the initial flow-induced orientation process. With an increasing MMT concentration (up to 50 wt %), the nanosheets became more and more confined with each other and thus have to stay highly oriented to accommodate neighboring nanosheets, leading to a much higher level of orientation. The above hypothesis was supported by both experimental (*34*–*36*) and modeling (*37*) explorations. When the MMT nanosheet concentration was further increased (that is, 60 and 70 wt %), the interlayer distance continued to shrink but the diffraction peaks became broader, suggesting that, overall, the nanosheets were less oriented in comparison to PVA/MMT-50-C. This is probably attributed to the significantly enhanced viscosity at such high concentration of nanosheets (*35*), which inhibits the nanosheets from rotating perfectly before the coating was dried and cross-linked.

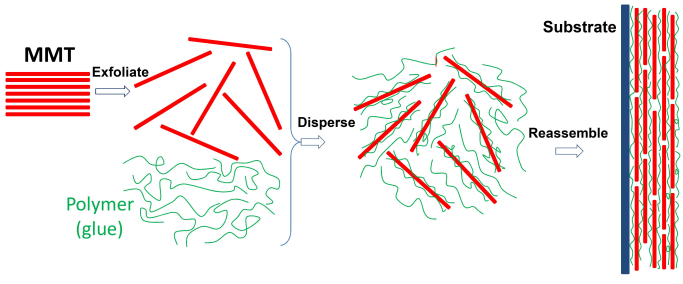

Fig. 1. Schematic of large-scale one-step coassembly. Flow-induced formation of a hybrid nanocoating with a well-oriented layered structure containing a high concentration of nanosheets (not drawn to scale).

Figure 3 shows the TEM images of the cross sections of the nanocoatings. Very consistent with the above XRD characterization, the images show variations of level of orientation and interlayer distance. Figure 3A shows the cross section of PVA/MMT-20-C. Although MMT nanosheets packed to form a roughly layered structure, overall, the nanosheets were not well aligned and sheet curvature was significant. For PVA/MMT-30-C (Fig. 3B), the MMT nanosheets were much better oriented with little curvature, but the variation in interlayer distance was still rather large (thus, a broad diffraction peak in Fig. 3). When the MMT concentration reached 50 wt %, the vast majority of the MMT nanosheets were very well aligned to be parallel to the substrate and were very well packed, and the interlayer distances were very close to each other (Fig. 3C and 4D). This is very consistent with its narrow and intense diffraction peak shown in Fig. 2. The grayscale analysis from a representative region in Fig. 3C shows that the interlayer distance is ca. 2.9 ± 0.2 nm, which is consistent with the XRD result. For PVA/MMT-60-C, the nanosheets were very closely packed, leading to an even lower interlayer distance, but their interlayer distance variation turned out to be larger. The nanosheets were overall not as well aligned as those in PVA/MMT-50-C, which is probably due to the high system viscosity that prevents the movement of nanosheets, as discussed above. A similar trend of nanosheet orientation was observed in PVA/MMT-70-C. Overall, the TEM images show a highly consistent morphology with what was revealed by their XRD patterns in terms of interlayer distance and level of orientation. The results showed that dozens of layers of MMT nanosheets can be well aligned via a very facile one-step coassembly process.

Although the TEM images noted above show only a tiny region (ca. 250 nm × 300 nm) of the observation of the nanosheet orientation, SAXS was used to statistically investigate the overall alignment

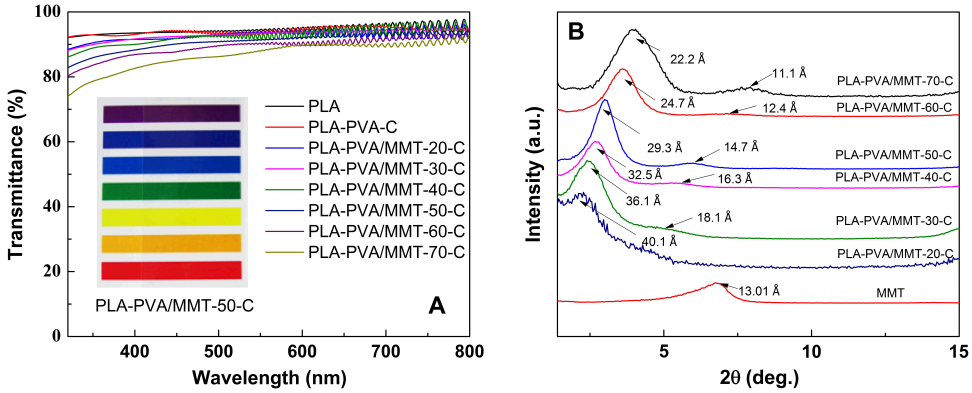

Fig. 2. UV-Vis and XRD characterization of the formed nanocoatings. (**A**) UV-Vis spectra and (**B**) XRD patterns of the coated PLA films. a.u., arbitrary units. The inset in (A) shows a digital image of PLA-PVA/MMT-50-C film placed above a printed rainbow pattern, exhibiting high transparency along the entire visible spectrum range.

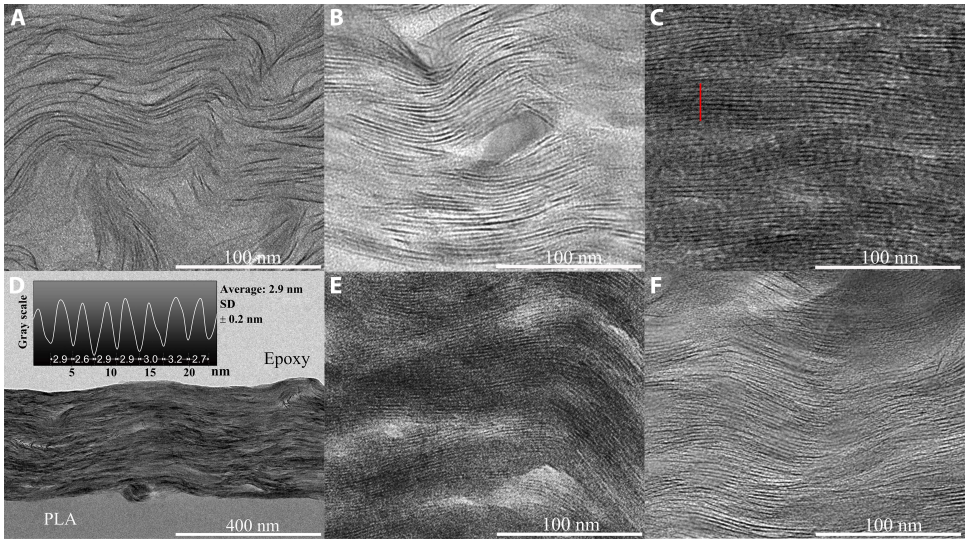

Fig. 3. TEM images of the cross section of the nanocoatings. (**A**) PVA/MMT-20-C. (**B**) PVA/MMT-30-C. (**C**) PVA/MMT-50-C. (**D**) PVA/MMT-50-C (low magnification); the inset shows the grayscale analysis of the interlayer distance along the red line marked in (C). (**E**) PVA/MMT-60-C. (**F**) PVA/MMT-70-C.

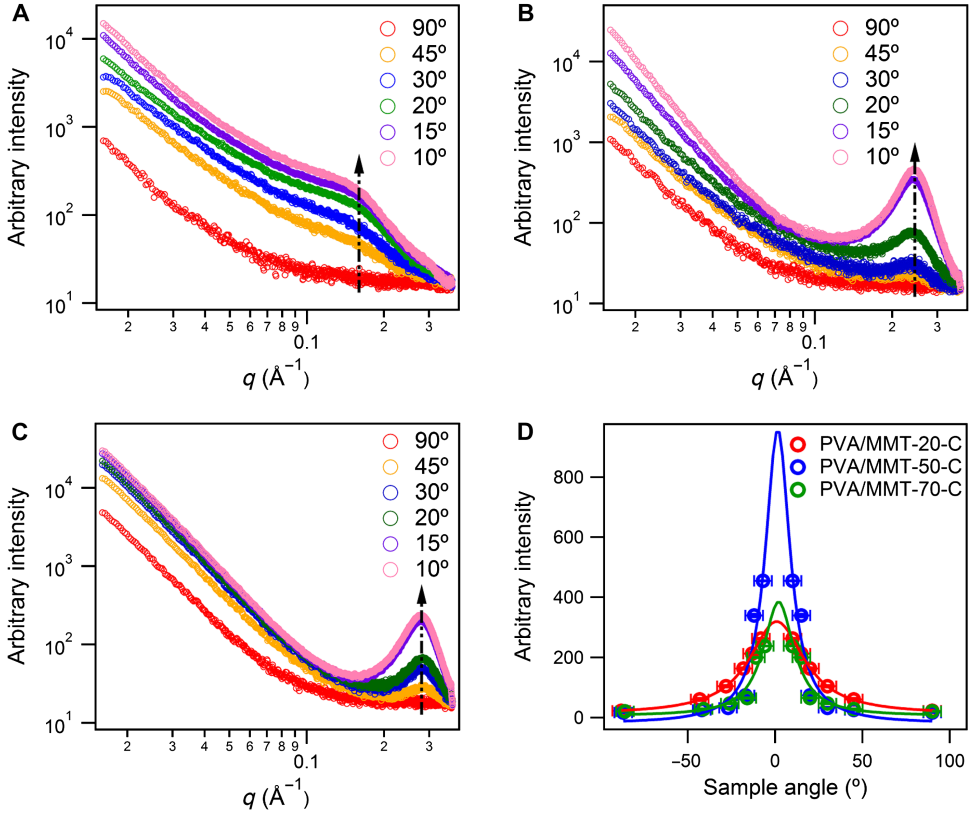

Fig. 4. SAXS patterns of the formed nanocoatings. (**A**) PVA/MMT-20-C. (**B**) PVA/MMT-50-C. (**C**) PVA/MMT-70-C. (**D**) Scattered intensity as a function of incident beam to sample angle, where solid lines are the best Lorentz fits. The R^2 values for the fitting for PVA/MMT-20-C, PVA/MMT-50-C, and PVA/MMT-70-C are 0.9997, 0.8912, and 0.8910, respectively.

of the nanosheets. Figure 4 (A to C) shows the one-dimensional (1D) SAXS patterns of PVA/MMT-20-C, PVA/MMT-50-C, and PVA/MMT-70-C, respectively, with the backgrounds being normalized on the basis of the corresponding data at φ = 90° when the incident beam was normal to the film surface, where no alignments were shown. The first-order Bragg peaks were observed from the SAXS profiles for all the samples, and the intensity at θ_B increased when the φ approaches the Bragg angle (black arrow). The rocking curve is presumably symmetric with respect to $\theta = \theta_B$. Therefore, to obtain a quantitative analysis of the alignment, we plotted the intensities

at $2\theta_B$ as a function of φ (Fig. 4D), which were then fitted using the Lorentz distribution as follows

$$I = I_0 + \frac{2A}{\pi}\frac{w}{4(\varphi - \theta_B)^2 + w^2} \quad (1)$$

where I_0 is the background, A is the area under the curve, and w is the full width at half maximum (FWHM). The fittings result in FWHMs of 38.5° ± 0.5°, 17.0° ± 6.2°, and 21.3° ± 6.3° for PVA/MMT-20-C, PVA/MMT-50-C, and PVA/MMT-70-C, respectively, indicating that PVA/MMT-50-C has the highest level of alignment, PVA/MMT-70-C is slightly lower, and PVA/MMT-20-C is the lowest, which is fully consistent with the XRD and TEM characterizations.

The above systematic characterizations have proven that we managed to assemble dozens of layers of MMT nanosheets per cycle of coating with a high efficiency. On the basis of this finding, cross-linking was used, including cross-linking the PVA chains and co–cross-linking the PVA chains with the MMT nanosheets, which have surface and edge hydroxyl groups (*22*). The aim of this procedure was to covalently incorporate the MMT nanosheets into the PVA matrix, forming a fully integrated system (Fig. 5).

To eliminate the interference from the PLA substrate, the nanocoating layers were delaminated from the PLA substrate for Fourier transform infrared (FTIR) characterization, and the results are presented in fig. S3. After cross-linking, there was a considerable reduction of the intensity of O–H peaks (ca. 3290 cm^{-1}) and C–OH peaks (ca. 1095 cm^{-1}) of PVA-C and PVA/MMT-50-C (*22*). An intensity increase of the peak at ca. 1377 cm^{-1} (C–O–C) of PVA-C and PVA/MMT-50-C from the formation of an acetal ring and ether linkage evidenced the reaction between the aldehydes and the hydroxyl groups on PVA (non–cross-linked PVA exhibiting a weak C–O–C peak due to the incomplete hydrolysis of acetyl groups) (*38*). The appearance of a new peak at ca. 1120 cm^{-1} in PVA/MMT-50-C is associated with the formation of Si–O–C bonds, suggesting the cross-linking between the MMT hydroxyl groups and glutaraldehyde (GA) (*22*). The above FTIR results support the cross-linking reactions. In addition, PVA and MMT can form another type of cyclic coupling between PVA and Al atoms on the surface and edge of MMT nanosheets without an extra cross-linking agent (*22*, *39*). This coupling, exhibited as a six-membered ring structure composed of one atom of Al and two atoms of O from MMT and three atoms of C from PVA, can be confirmed by the appearance of an Al–O–C vibration peak at 848 cm^{-1} (*29*). Moreover, PVA and MMT can form strong epitaxial hydrogen bonding (*22*). More details of the spectra interpretation that further support the above claims are included in the Supplementary Materials. The above cross-linking and hydrogen bonding are expected to effectively integrate MMT nanosheets into the PVA matrix to form a highly cross-linked structure, which should effectively enforce load transfer and thus improve mechanical properties. The significantly improved interface is also very valuable for barrier property improvement.

Mechanical properties of the hybrid nanocoatings

Because of the achievement of a high concentration, a high level of dispersion and orientation of MMT nanosheets, and co–cross-linking between MMT and PVA, these nanocoatings exhibit outstanding mechanical properties. The key tensile test results are listed in Table 1, and the representative tensile curves are shown in Fig. 5. With an increasing concentration of MMT nanosheets, the nanocoatings exhibited a marked increase in both tensile strength and modulus (Fig. 5C). Meanwhile, the cross-linked nanocoatings exhibited a much higher mechanical performance compared to the non–cross-linked ones, because the cross-linking provides a much more effective load transfer (Fig. 5D). At a loading of 50 wt % of MMT, the tensile strength of PVA/MMT-50-C is ca. 171% of aerospace grade aluminum alloy 2014 (*40*) and ca. 60% of stainless steel. Also, the modulus of PVA/MMT-50-C is very close to that of aluminum alloy 2014. Considering that the density of PVA/MMT-50-C is only 1.75 (see table S1 for details), its specific modulus and strength are thus much higher than

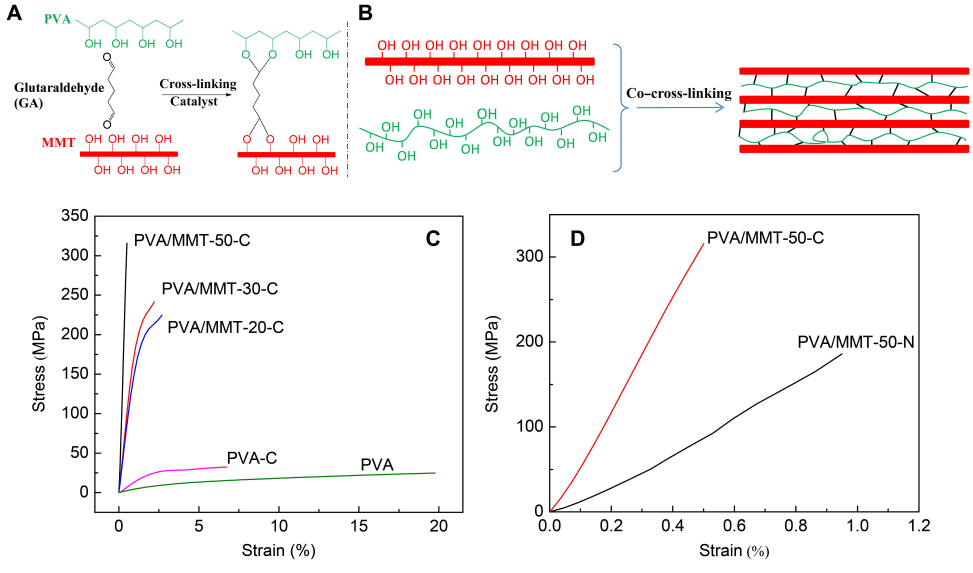

Fig. 5. Integration of the PVA/MMT nanocoatings and mechanical properties of the freestanding films. (**A**) Cross-linking reaction between PVA and MMT using GA. (**B**) Schematic of the formation of an integrated structure after the co–cross-linking between MMT nanosheets and PVA chains. Representative stress–strain curves of (**C**) freestanding film samples with various MMT concentrations and (**D**) freestanding film samples with and without cross-linking.

Table 1. Mechanical properties of the freestanding nanocoatings. The Mechanical property data of aluminum alloy and stainless steel for comparison are from bulky materials.

Sample	Tensile strength (MPa)	Young's modulus (GPa)	Strain (%)	Density (g/cm^3)	Specific strength (MPa·cm^3/g)	Specific modulus (GPa·cm^3/g)
PVA	24.8 ± 2.2	0.5 ± 0.1	19.8 ± 2.3	—	—	—
PVA-C	32.3 ± 2.6	1.5 ± 0.2	6.7 ± 0.8	—	—	—
PVA/MMT-20-C	224.6 ± 18.6	16.8 ± 2.1	2.7 ± 0.5	1.43	158	11.8
PVA/MMT-30-C	241.4 ± 24.1	20.0 ± 2.8	2.2 ± 0.3	1.52	159	13.2
PVA/MMT-50-N	185.9 ± 20.6	20.0 ± 2.5	1.0 ± 0.2	1.75	106	11.5
PVA/MMT-50-C	315.7 ± 28.2	65.0 ± 4.8	0.5 ± 0.1	1.75	181	37.2
Nacre	80–135 (*52*)	60–70 (*52*)	0.2–0.9 (*52*, *53*)	2.65 (*54*)	30.2–50.9	22.6–26.4
Aluminum alloy 2014 (annealed) (*55*)	185	70	—	2.73	67.8	26
Stainless steel type 304 (*55*)	550	195	—	7.90	69.6	25

those of stainless steel. The key mechanical properties are plotted in fig. S4 to help visualize the relative performances of each material. The nanocoating with 50 wt % of MMT is stronger but more fragile in comparison to nacre.

Barrier properties of coated films

Because of the high level of orientation and the very dense packing of MMT nanosheets, these nanocoatings also exhibited an outstanding barrier performance, as shown in Table 2. The PLA films (20 μm) exhibited a high oxygen transmission rate (OTR) of 1205.0 ml/(m^2·day). After being coated with a thin layer of PVA-C (255 nm) on both sides, the OTR of the coated PLA films was lowered to 7.4 ml/(m^2·day). With the incorporation of 20 wt % of MMT nanosheets, the OTR of PLA-PVA/MMT-20-C was further lowered to 3.6 ml/(m^2·day). At 50 wt % of MMT, the cross-linked nanocoating helped lower the OTR to 0.2 ml/(m^2·day). The OTR of PLA-PVA/MMT-70-C was detected as 0.1 ml/(m^2·day), representing a decrease of approximately four orders of magnitude compared to the neat PLA film. Note that the above OTR data did not take the coating thickness into consideration. By calculating the O_2 permeability based on the unit film thickness of both the coated film and the coating layer only, one can observe an even more distinctive barrier performance of the nanocoating, considering that the coating thickness is in the 560- to 650-nm range, whereas the substrate film is much thicker (20 μm). Alternatively, the barrier improvement factor (BIF) (*41*) (which is defined as P_s/P_t, where P_s is the permeability of the substrate and P_t is the permeability of the coated substrate) can be used to assess the overall barrier performance of the coating. As shown in Table 2, the BIF of the coated PLA films reached 13,765 when the nanocoating contained 70 wt % of MMT. In contrast, SiO_x thin film, a widely accepted high-performance oxygen barrier coating, has a BIF of 500 (*42*).

The WVTR of the coated PLA films was decreased greatly as well, but to a lesser degree compared to the OTR of the coated PLA films, which can be attributed to the hydrophilic nature of both PLA and MMT. Similar barrier performance was achieved on PET, BOPP, HDPE, and LDPE films, as shown in Table 2. The results show that the PVA/MMT nanocoating is especially ideal for polyolefin (BOPP, HDPE, and LDPE) films, which inherently have excellent moisture barrier properties but are a very poor oxygen barrier (*43*, *44*). The PVA-based nanocoating perfectly supplements the need of polyolefin films to achieve an outstanding barrier to both oxygen and moisture.

Flame-retardant property of coated parts

Because the hundreds of layers of densely packed nanosheets led to superior gas barrier properties, such a structure should be able to significantly lower heat and oxygen transfer and thus might be effective in flame retardation as well. Considering that PET is a very flammable plastic and widely used in our daily life (*45*), a vertical combustibility test was conducted on the coated PET films. Upon ignition, the non-coated PET films were burned very quickly and dripped severely (see movie S1). However, the coated films (PET-PVA/MMT-50-C) could barely be ignited (see movie S2). After 30 s of combustion, the films maintained their original dimension (Fig. 6C). The scanning electron microscopy (SEM) images of the cross section of the coating layer before and after the combustibility test (Fig. 6, A and B, respectively) show that the MMT nanosheets remained to be closely packed after the combustibility test, although the interlayer distance turned to be slightly larger. This is probably due to the degradation of the PVA within the MMT layers, leading to a slight layer-layer expansion, which would improve the flame resistance as does an intumescent coating. This dense coverage composed of hundreds of layers of MMT is believed to be the reason for its outstanding flame-retardant property.

The flame retardancy performance of the nanocoatings was further evaluated on highly flammable open-cell polyurethane (PU) foams, which were coated by soaking the foams in a dispersion followed by gently shaking off excessive dispersion, and finally dried in an oven. The goal is to form a thin layer of nanocoating on the cell walls of the foam, which is expected to serve a similar function as on PET films. The formation of a thin layer of nanocoating was supported by the SEM images of the PU foam cell wall before and after coating treatment (fig. S5). After 10 s of horizontal combustibility test (*46*), the neat PU foam sample was almost consumed, with only a small piece of debris left (Fig. 6, D and E, and movie S3). On the other end, the coated PU foam sample (PU-PVA/MMT-50-C) exhibited outstanding flame retardancy. Only the zone in contact with

Table 2. Barrier properties of the coated plastic films. All films were coated on both sides. The number of MMT layers was estimated on the basis of the coating thickness and the interlayer distance of the MMT layers from the corresponding XRD patterns. WVTR, water vapor transmission rate; BOPP, biaxially oriented polypropylene; HDPE, high-density polyethylene; LDPE, low-density polyethylene; STP, standard temperature and pressure; PET, polyethylene terephthalate.

Formulation in graft	Nanocoating thickness (nm)	Number of clay layers	WVTR [g/(m^2·day)]	OTR [ml/(m^2·day)]	O_2 permeability of coated film [10^{-16} cm^3(STP)·cm/cm^2·s·Pa]	O_2 permeability of coating layer [10^{-16} cm^3(STP)·cm/cm^2·s·Pa]	BIF
PLA (20 μm)	—	—	98.2	1205.0	275.29	—	—
PLA-PVA	450 ± 25	—	34.8	9.4	2.20	0.0488	125
PLA-PVA-C	510 ± 26	—	31.4	7.4	1.73	0.0433	159
PLA-PVA/MMT-20-C	560 ± 34	140 ± 8	26.4	3.6	0.85	0.0232	324
PLA-PVA/MMT-30-C	600 ± 30	166 ± 8	18.9	1.5	0.35	0.0102	787
PLA-PVA/MMT-40-C	608 ± 24	187 ± 7	14.5	0.6	0.14	0.0041	1966
PLA-PVA/MMT-50	590 ± 32	220 ± 12	17.2	0.2	0.05	0.0014	5506
PLA-PVA/MMT-50-C	620 ± 23	212 ± 8	13.1	0.2	0.05	0.0015	5506
PLA-PVA/MMT-60	610 ± 24	260 ± 10	15.6	0.2	0.05	0.0015	5506
PLA-PVA/MMT-60-C	620 ± 31	251 ± 13	10.9	0.2	0.05	0.0015	5506
PLA-PVA/MMT-70-C	650 ± 25	293 ± 11	10.1	0.1	0.02	0.0006	13765
PET (24 μm)	—	—	4.1	64.0	16.08	—	—
PET-PVA-C	596 ± 29	—	3.1	14.8	3.82	0.1311	4
PET-PVA/MMT-50-C	625 ± 20	213 ± 7	2.6	0.1	0.03	0.0008	585
BOPP (20 μm)	—	—	1.1	1860.0	424.93	—	—
BOPP-PVA-C	570 ± 30	—	0.4	45.0	10.57	0.3002	40
BOPP-PVA/MMT-50-C	615 ± 25	210 ± 8	0.6	0.2	0.05	0.0015	8499
HDPE (25.4 μm)	—	—	0.6	2530.0	734.05	—	—
HDPE-PVA-C	625 ± 33	—	0.4	33.0	9.81	0.2387	75
HDPE-PVA/MMT-50-C	680 ± 26	239 ± 9	0.5	0.4	0.12	0.0031	6117
LDPE (25.4 μm)	—	—	2.1	4050.0	1175.06	—	—
LDPE-PVA-C	600 ± 28	—	1.7	40.8	12.12	0.2825	97
LDPE-PVA/MMT-50-C	625 ± 22	213 ± 7	1.3	0.1	0.03	0.0007	39169

the ignition flame was briefly burned (Fig. 6, F and G, and movie S4). Other sections barely changed color or shape. During combustion, the MMT nanosheets served as protective layers to prevent oxygen and heat from entering the PU substrate. During surface combustion, the MMT nanosheets accumulated with the carbonaceous char generated by PVA and PU, and this mixture consisting of MMT and carbonaceous char suppressed and trapped the rising gases from the decomposition of PU foam, forming a bubble structure between the unburned PU foam and the mixed char. This double block can efficiently suppress the transport of heat and oxygen, effectively protecting the unburned PU foam (*47*, *48*).

DISCUSSION

The above systematic characterizations have proven that we managed to assemble and align dozens of layers of MMT nanosheets per cycle of coating with a high efficiency, which can probably be attributed to three causes: (i) The flow helps to induce initial and rough orientation; (ii) the highly crowded nanosheets force themselves to remain highly oriented with each other to accommodate neighboring ones before the coating is dried; and (iii) the final drying process further helps align the nanosheets (fig. S6A). A control experiment was conducted to prepare a PVA/MMT-50-C nanocoating by horizontally casting the same dispersion on the same film substrate. The XRD pattern of the resultant nanocoating is shown in fig. S6B, which showed a broader peak but a similar interlayer distance in comparison to the one prepared vertically with flow. This horizontally coated film also exhibited a much higher O_2 permeability of 8.3×10^{-19} cm^3(STP)·cm/cm^2·s·Pa, more than five times higher than that of the vertically coated one. These results further suggest that the initial flow-induced orientation is very critical for the alignment of nanosheets in the entire nanocoating formation. Another disadvantage of the conventional horizontal casting method is that it is more difficult to achieve continuous large-scale

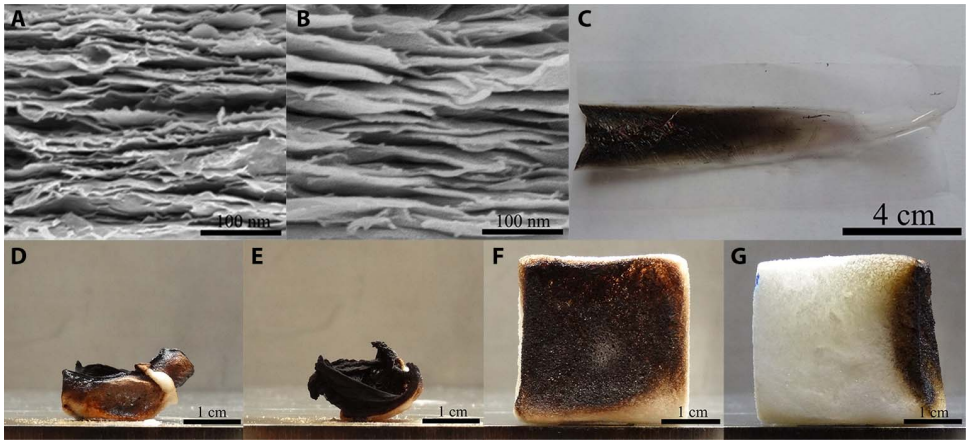

Fig. 6. Flame-retardant performance of the coated parts. SEM images of the cross section of PVA/MMT-50-C before (**A**) and after (**B**) vertical combustibility testing; digital image of the PET-PVA/MMT-50-C film after 30 s of vertical combustibility testing (**C**). Digital image of the neat PU foam after horizontal combustibility testing: front view (**D**) and side view (**E**). Digital image of the treated PU foam after horizontal combustibility testing: front view (**F**) and side view (**G**).

fabrication, whereas the vertical casting process can be easily scaled up for mass production. Although LbL can continuously achieve uniform thin films, it is much more complicated.

In summary, we have developed a facile and effective self-assembly process to form nanocoatings with a nacre-like structure. This new coating process has no limit on lateral dimensions but can only coat to form thin films. Dozens of nanosheets could be well assembled and aligned during each coating cycle, in high contrast to the LbL technique that can assemble only one layer during each cycle (*21*). This approach can be easily adopted to be a continuous process (for example, a moving plastic film through a liquid container) for mass production. The composition of the final nanocoating can be easily adjusted, leading to a high composition flexibility and property tunability. The nanocoatings exhibited outstanding mechanical, barrier, and flame-retardant properties, promising for widespread application.

MATERIALS AND METHODS

Materials

PVA [Mowiol 8-88; M_w (weight average molecular weight): 67,000, 86.7 to 88.7 mole percent hydrolysis; Kuraray], sodium MMT (Cloisite Na^+, BYK Additives Inc.), GA (50% aqueous solution; Sigma-Aldrich), and HCl (37%; Sigma-Aldrich) were used as received without further purification.

Various polymer films were used as the coating substrates. PLA films with a thickness of 20 μm were obtained from BI-AX International Inc. PET films with a thickness of 24 μm and BOPP films with a thickness of 20 μm were obtained from Toray Plastics (America) Inc. HDPE (25.4 μm) and LDPE (25.4 μm) cast films were obtained from Berry Plastics Corporation. Open-cell PU foam with a density of 12.7 kg/m^3 was obtained from Huntsman Corporation. PLA and PET films, as well as PU foams, were used as received, whereas BOPP, HDPE, and LDPE films were plasma-treated (Plasma Gas System 210, PVA TePla America; oxygen flow rate, 20 standard cubic centimeters per minute; pressure, 150 mtorr; 300 W) for 4 min immediately before the coating process.

Preparation of PVA/MMT dispersion

PVA was dissolved in deionized (DI) water with the assistance of brief heating. MMT was uniformly dispersed in DI water with the assistance of stirring, followed by 30 min of ultrasonication in an ultrasonication bath (Branson 8510R-MT, 250 W, 44 kHz) (*22*). The PVA solution was added to the MMT aqueous dispersion to form a dispersion system containing 1.5 wt % of total solids (MMT + PVA) and 98.5 wt % of water. The mixture was stirred for 30 min and briefly ultrasonicated to ensure a uniform dispersion. A small amount of cross-linking agent GA was added to the mixture, whose mole ratio to the total mole number of hydroxyl groups on PVA chains was 1:20. HCl was used as the catalyst for the cross-linking reaction, whose mole ratio to GA was 1:5.

Preparation of PVA/MMT hybrid nanocoatings

The PLA (or other polymer) films (ca. 15 cm × 20 cm) were facilely coated by dipping them into the above aqueous dispersion for ca. 10 s and then vertically hung in an oven to be dried and cross-linked at 60°C. The coating process was repeated four times with an aim to obtain sufficiently thick coatings for handling and testing. To maintain an even coating layer on the film surface, the film was rotated 180° before the next cycle of dip coating. The coated samples were labeled as PLA (or other polymer)–PVA/MMT-*X*-C (*X* is the mass percentage of MMT in the mixture of MMT and PVA in the initial formulation; C refers to cross-linked). Non–cross-linked samples (without GA) were also prepared as a control and labeled as PLA (or other polymer)–PVA/MMT-*X*-N (N refers to "non–cross-linked"). The freestanding hybrid thin films were delaminated from the substrate using Scotch tape, similar to the method used to peel graphene from graphite, for various characterizations (*49*).

The PU foam was first cut into cubes (ca. 0.0254 m × 0.0254 m × 0.0254 m). The cubes were coated by soaking the specimens in the above aqueous dispersion for ca. 5 min, followed by gently shaking off excessive dispersion, and finally dried in an oven at 60°C.

Characterization

The UV-Vis spectra of the coated PLA samples were recorded using a UV-Vis spectrophotometer (Lambda 900, PerkinElmer). The FTIR spectroscopy spectra were recorded on a PerkinElmer Spectrum 100 spectrophotometer using freestanding hybrid thin films.

The XRD patterns were recorded on a Bruker D8 diffractometer with Bragg-Brentano θ-2θ geometry using a graphite monochromator with Cu Kα radiation. The coated PLA samples were used for XRD characterization.

SEM images were acquired on an FEI Strata 400S field emission–SEM. The samples were sputter-coated with a thin layer (ca. 3 nm) of Au/Pd before SEM imaging.

To capture the cross section of the nanocoating layers, we embedded the coated PLA films into epoxy, which were microtomed into thin slices with a thickness of 80 to 100 nm on a Reichert-Jung Ultracut E ultramicrotome. The thin sections were deposited on 400-mesh copper grids for imaging under a JEOL JEM 1200 EXII TEM with an accelerating voltage of 120 kV.

SAXS measurements were conducted at a Bruker NanoSTAR instrument. X-ray was generated by a Turbo (rotating anode) x-ray source. A wavelength of 1.5418 Å was chosen by Cu Kα using the Göbel mirror. The beam was collimated by a pair of scatterless pinholes with diameters of 500 and 350 μm. The 2D intensity data were collected using a MikroGap VÅNTEC-2000 detector with a sample-to-detector distance of 67 cm to cover a scattering vector, $\boldsymbol{q}$ [$|q| \equiv \frac{4\pi}{\lambda}\sin(\frac{\theta}{2})$, where θ is the scattering angle], ranging from 0.015 to 0.37 $Å^{-1}$. To investigate the lamellar alignments for different samples, we conducted rocking curve experiments on SAXS, which reports the distribution of the domains misoriented from the perfect orientation [that is, φ (the angle between the incident beam and sample) = θ_B, where θ_B is the Bragg angle]. By manually rotating the sample to different φ, the 2D scattering patterns were collected at different φ values, which were then corrected for the background and reduced to 1D data after a sector integration due to the anisotropy of the 2D data. The range for the sector integrations was set to be the same at different φ values for the same sample. The thickness of the nanocoatings was measured using a Veeco Dektak 150 surface profilometer.

Static uniaxial tensile tests were conducted on a dynamic mechanical analyzer (DMA Q800, TA Instruments) (*50*) at 22°C and 30% relative humidity (RH). The regular freestanding hybrid thin films are too thin (ca. 300 nm in thickness, as shown in Table 2) for accurate mechanical testing. Thus, some thick hybrid films were intentionally prepared for mechanical testing by increasing the coating process to eight cycles using a PET film as the substrate. After they were dried and cross-linked, the freestanding nanocoating layers were delaminated from the substrate using Scotch tape (*49*). Note that the stiffness and strength of the eight-cycle hybrid films should be the same as the four-cycle hybrid films in theory. The purpose of preparing these thick hybrid films was only for better handling and more accurate testing result. The freestanding hybrid films were cut into rectangular strips of 4 mm × 30 mm for mechanical testing. The specimens were first dried in an oven at 105°C for 5 hours and then were equilibrated under 22°C and 30% RH for 24 hours before mechanical testing. All the tensile tests were conducted in the controlled strain rate mode with a preload of 0.001 N and a strain ramp rate of 10.0%/min. At least 10 specimens were tested for each sample, and the average results were reported.

OTRs were tested on a MOCON OX-TRAN 1/50 OTR tester at 23°C and 0% RH following ASTM D3985. WVTRs were tested on a MOCON PERMATRAN-W 1/50 WVTR tester at 23°C and 50% RH following ASTM E398.

Flammability of the coated PET films was evaluated by the vertical combustibility test method modified from ASMT D6413 (*51*), as demonstrated in the attached movies. Flammability of the coated PU foams was evaluated by horizontally exposing the foam samples to direct flame from a butane torch (Model Weller ML200, Apex Tool Group, Apex, NC 27539-8160) for 10 s (the approximate flame temperature is 1300°C according to the vendor) (*46*). The flammability testing process was recorded on a Sony DSC-HX9V camera.

SUPPLEMENTARY MATERIALS

Supplementary material for this article is available at http://advances.sciencemag.org/cgi/content/full/3/7/e1701212/DC1

fig. S1. SEM image of a nacre acquired on a pearl.
fig. S2. Dimensions of MMT nanosheets.
fig. S3. Characterization of the integrated PVA/MMT nanocoatings.
fig. S4. Comparison of mechanical properties of the materials.
fig. S5. Surface morphology of the noncoated and coated PU foams.
fig. S6. Comparison of horizontal and vertical casting.
table S1. Estimated density of the nanocoatings.
movie S1. Vertical combustibility testing of the noncoated PET film.
movie S2. Vertical combustibility testing of the coated PET film.
movie S3. Horizontal combustibility testing of the noncoated PU foam.
movie S4. Horizontal combustibility testing of the coated PU foam.
References (*56*–*60*)

REFERENCES AND NOTES

1. B. R. Heywood, S. Mann, Template-directed nucleation and growth of inorganic materials. *Adv. Mater.* **6**, 9–20 (1994).
2. L. Addadi, S. Weiner, Biomineralization: A pavement of pearl. *Nature* **389**, 912–915 (1997).
3. M. Darder, P. Aranda, E. Ruiz-Hitzky, Bionanocomposites: A new concept of ecological, bioinspired, and functional hybrid materials. *Adv. Mater.* **19**, 1309–1319 (2007).
4. G. Mayer, Rigid biological systems as models for synthetic composites. *Science* **310**, 1144–1147 (2005).
5. J. D. Currey, Mechanical properties of mother of pearl in tension. *Proc. R. Soc. London Ser. B* **196**, 443–463 (1977).
6. S. Deville, E. Saiz, R. K. Nalla, A. P. Tomsia, Freezing as a path to build complex composites. *Science* **311**, 515–518 (2006).
7. C. Sanchez, H. Arribart, M. M. G. Guille, Biomimetism and bioinspiration as tools for the design of innovative materials and systems. *Nat. Mater.* **4**, 277–288 (2005).
8. F. Barthelat, Biomimetics for next generation materials. *Philos. Trans. A Math. Phys. Eng. Sci.* **365**, 2907–2919 (2007).
9. H. D. Espinosa, J. E. Rim, F. Barthelat, M. J. Buehler, Merger of structure and material in nacre and bone—Perspectives on de novo biomimetic materials. *Prog. Mater. Sci.* **54**, 1059–1100 (2009).
10. M. A. Meyers, P.-Y. Chen, A. Y.-M. Lin, Y. Seki, Biological materials: Structure and mechanical properties. *Prog. Mater. Sci.* **53**, 1–206 (2008).
11. M. Cusack, A. Freer, Biomineralization: Elemental and organic influence in carbonate systems. *Chem. Rev.* **108**, 4433–4454 (2008).
12. H.-B. Yao, H.-Y. Fang, X.-H. Wang, S.-H. Yu, Hierarchical assembly of micro-/nano-building blocks: Bio-inspired rigid structural functional materials. *Chem. Soc. Rev.* **40**, 3764–3785 (2011).
13. G. M. Luz, J. F. Mano, Biomimetic design of materials and biomaterials inspired by the structure of nacre. *Philos. Trans. A Math. Phys. Eng. Sci.* **367**, 1587–1605 (2009).
14. L. Addadi, D. Joester, F. Nudelman, S. Weiner, Mollusk shell formation: A source of new concepts for understanding biomineralization processes. *Chem. Eur. J.* **12**, 980–987 (2006).
15. F. C. Meldrum, H. Cölfen, Controlling mineral morphologies and structures in biological and synthetic systems. *Chem. Rev.* **108**, 4332–4432 (2008).
16. A. P. Jackson, J. F. V. Vincent, R. M. Turner, The mechanical design of nacre. *Proc. R. Soc. London Ser. B* **234**, 415–440 (1988).
17. L.-B. Mao, H.-L. Gao, H.-B. Yao, L. Liu, H. Cölfen, G. Liu, S.-M. Chen, S.-K. Li, Y.-X. Yan, Y.-Y. Liu, S.-H. Yu, Synthetic nacre by predesigned matrix-directed mineralization. *Science* **354**, 107–110 (2016).
18. M. E. Launey, E. Munch, D. H. Alsem, E. Saiz, A. P. Tomsia, R. O. Ritchie, A novel biomimetic approach to the design of high-performance ceramic–metal composites. *J. R. Soc. Interface* **7**, 741–753 (2010).
19. M. A. Priolo, D. Gamboa, K. M. Holder, J. C. Grunlan, Super gas barrier of transparent polymer–clay multilayer ultrathin films. *Nano Lett.* **10**, 4970–4974 (2010).
20. Y.-C. Li, S. Mannen, A. B. Morgan, S. Chang, Y.-H. Yang, B. Condon, J. C. Grunlan, Intumescent all-polymer multilayer nanocoating capable of extinguishing flame on fabric. *Adv. Mater.* **23**, 3926–3931 (2011).
21. P. Bertrand, A. Jonas, A. Laschewsky, R. Legras, Ultrathin polymer coatings by complexation of polyelectrolytes at interfaces: Suitable materials, structure and properties. *Macromol. Rapid Commun.* **21**, 319–348 (2000).
22. P. Podsiadlo, A. K. Kaushik, E. M. Arruda, A. M. Waas, B. S. Shim, J. Xu, H. Nandivada, B. G. Pumplin, J. Lahann, A. Ramamoorthy, N. A. Kotov, Ultrastrong and stiff layered polymer nanocomposites. *Science* **318**, 80–83 (2007).
23. B. Long, C.-A. Wang, W. Lin, Y. Huang, J. Sun, Polyacrylamide-clay nacre-like nanocomposites prepared by electrophoretic deposition. *Compos. Sci. Technol.* **67**, 2770–2774 (2007).

24. T. D. Papathanasiou, D. C. Guell, *Flow-Induced Alignment in Composite Materials* (Woodhead Publishing Limited, 1997).
25. B. Su, X. Lu, Q. Lu, A facile method to prepare macroscopically oriented mesostructured silica film: Controlling the orientation of mesochannels in multilayer films by air flow. *J. Am. Chem. Soc.* **130**, 14356–14357 (2008).
26. D. E. Kataoka, S. M. Troian, Patterning liquid flow on the microscopic scale. *Nature* **402**, 794–797 (1999).
27. H. J. Ploehn, C. Liu, Quantitative analysis of montmorillonite platelet size by atomic force microscopy. *Ind. Eng. Chem. Res.* **45**, 7025–7034 (2006).
28. P. F. Luckham, S. Rossi, The colloidal and rheological properties of bentonite suspensions. *Adv. Colloid Interface Sci.* **82**, 43–92 (1999).
29. D. J. Greenland, Adsorption of polyvinyl alcohols by montmorillonite. *J. Colloid Sci.* **18**, 647–664 (1963).
30. D. Z. Gunes, R. Scirocco, J. Mewis, J. Vermant, Flow-induced orientation of non-spherical particles: Effect of aspect ratio and medium rheology. *J. Nonnewton. Fluid Mech.* **155**, 39–50 (2008).
31. Y. Guan, S. Yang, Y. Zhang, J. Xu, C. C. Han, N. A. Kotov, Fabry–Perot fringes and their application to study the film growth, chain rearrangement, and erosion of hydrogen-bonded PVPON/PAA films. *J. Phys. Chem. B* **110**, 13484–13490 (2006).
32. Y.-H. Yu, C.-Y. Lin, J.-M. Yeh, W.-H. Lin, Preparation and properties of poly(vinyl alcohol)–clay nanocomposite materials. *Polymer* **44**, 3553–3560 (2003).
33. Y. Deng, A. Gu, Z. Fang, The effect of morphology on the optical properties of transparent epoxy/montmorillonite composites. *Polym. Int.* **53**, 85–91 (2004).
34. H.-J. Sue, K. T. Gam, N. Bestaoui, N. Spurr, A. Clearfield, Epoxy nanocomposites based on the synthetic α-zirconium phosphate layer structure. *Chem. Mater.* **16**, 242–249 (2003).
35. L. Sun, W.-J. Boo, J. Liu, A. Clearfield, H.-J. Sue, N. E. Verghese, H. Q. Pham, J. Bicerano, Effect of nanoplatelets on the rheological behavior of epoxy monomers. *Macromol. Mater. Eng.* **294**, 103–113 (2009).
36. L. Sun, W.-J. Boo, A. Clearfield, H.-J. Sue, H. Q. Pham, Barrier properties of model epoxy nanocomposites. *J. Membr. Sci.* **318**, 129–136 (2008).
37. J. Bicerano, J. F. Douglas, D. A. Brune, Model for the viscosity of particle dispersions. *J. Macromol. Sci. Polym. Rev.* **39**, 561–642 (1999).
38. C.-K. Yeom, K.-H. Lee, Pervaporation separation of water-acetic acid mixtures through poly(vinyl alcohol) membranes crosslinked with glutaraldehyde. *J. Membr. Sci.* **109**, 257–265 (1996).
39. A. Amore Bonapasta, F. Buda, P. Colombet, Cross-linking of poly(vinyl alcohol) chains by Al ions in macro-defect-free cements: A theoretical study. *Chem. Mater.* **12**, 738–743 (2000).
40. J. C. Williams, E. A. Starke Jr., Progress in structural materials for aerospace systems. *Acta Mater.* **51**, 5775–5799 (2003).
41. M. A. Priolo, K. M. Holder, D. Gamboa, J. C. Grunlan, Influence of clay concentration on the gas barrier of clay–polymer nanobrick wall thin film assemblies. *Langmuir* **27**, 12106–12114 (2011).
42. A. Grüniger, A. Bieder, A. Sonnenfeld, P. R. von Rohr, U. Müller, R. Hauert, Influence of film structure and composition on diffusion barrier performance of SiO_x thin films deposited by PECVD. *Surf. Coat. Technol.* **200**, 4564–4571 (2006).
43. C. F. Struller, P. J. Kelly, N. J. Copeland, Aluminum oxide barrier coatings on polymer films for food packaging applications. *Surf. Coat. Technol.* **241**, 130–137 (2014).
44. T. Hirvikorpi, M. Vähä-Nissi, A. Harlin, J. Marles, V. Miikkulainen, M. Karppinen, Effect of corona pre-treatment on the performance of gas barrier layers applied by atomic layer deposition onto polymer-coated paperboard. *Appl. Surf. Sci.* **257**, 736–740 (2010).
45. S. V. Levchik, E. D. Weil, A review on thermal decomposition and combustion of thermoplastic polyesters. *Polym. Adv. Technol.* **15**, 691–700 (2004).
46. D. Patra, P. Vangal, A. A. Cain, C. Cho, O. Regev, J. C. Grunlan, Inorganic nanoparticle thin film that suppresses flammability of polyurethane with only a single electrostatically-assembled bilayer. *ACS Appl. Mater. Interfaces* **6**, 16903–16908 (2014).
47. T. Guin, M. Krecker, A. Milhorn, D. A. Hagen, B. Stevens, J. C. Grunlan, Exceptional flame resistance and gas barrier with thick multilayer nanobrick wall thin films. *Adv. Mater. Interfaces* **2**, 1500214 (2015).
48. R. Davis, Y.-C. Li, M. Gervasio, J. Luu, Y. S. Kim, One-pot, bioinspired coatings to reduce the flammability of flexible polyurethane foams. *ACS Appl. Mater. Interfaces* **7**, 6082–6092 (2015).
49. K. S. Novoselov, A. K. Geim, S. V. Morozov, D. Jiang, Y. Zhang, S. V. Dubonos, I. V. Grigorieva, A. A. Firsov, Electric field effect in atomically thin carbon films. *Science* **306**, 666–669 (2004).
50. H. Chen, M. B. Müller, K. J. Gilmore, G. G. Wallace, D. Li, Mechanically strong, electrically conductive, and biocompatible graphene paper. *Adv. Mater.* **20**, 3557–3561 (2008).
51. F. Carosio, G. Laufer, J. Alongi, G. Camino, J. C. Grunlan, Layer-by-layer assembly of silica-based flame retardant thin film on PET fabric. *Polym. Degrad. Stab.* **96**, 745–750 (2011).
52. J. Wang, Q. Cheng, Z. Tang, Layered nanocomposites inspired by the structure and mechanical properties of nacre. *Chem. Soc. Rev.* **41**, 1111–1129 (2012).
53. F. Barthelat, H. Tang, P. D. Zavattieri, C.-M. Li, H. D. Espinosa, On the mechanics of mother-of-pearl: A key feature in the material hierarchical structure. *J. Mech. Phys. Solids* **55**, 306–337 (2007).
54. G. E. G. Westermann, Hydrostatics, propulsion and life-habits of the Cretaceous ammonoid Baculites. *Rev. Paleobiol.* **32**, 249–265 (2013).
55. R. D. Lide, Properties of commercial metals and alloys, in *CRC Handbook of Chemistry and Physics* (CRC Press, Taylor and Francis, ed. 92, 2010), pp. 12–224.
56. H. S. Mansur, C. M. Sadahira, A. N. Souza, A. A. P. Mansur, FTIR spectroscopy characterization of poly (vinyl alcohol) hydrogel with different hydrolysis degree and chemically crosslinked with glutaraldehyde. *Mater. Sci. Eng. C* **28**, 539–548 (2008).
57. H. S. Mansur, R. L. Oréfice, A. A. P. Mansur, Characterization of poly(vinyl alcohol)/poly(ethylene glycol) hydrogels and PVA-derived hybrids by small-angle X-ray scattering and FTIR spectroscopy. *Polymer* **45**, 7193–7202 (2004).
58. C. M. Paranhos, B. G. Soares, R. N. Oliveira, L. A. Pessan, Poly(vinyl alcohol)/clay-based nanocomposite hydrogels: Swelling behavior and characterization. *Macromol. Mater. Eng.* **292**, 620–626 (2007).
59. J. E. Mark, *Polymer Data Handbook* (Oxford Univ. Press, 1999).
60. J. P. G. Villaluenga, M. Khayet, M. A. López-Manchado, J. L. Valentin, B. Seoane, J. I. Mengual, Gas transport properties of polypropylene/clay composite membranes. *Eur. Polym. J.* **43**, 1132–1143 (2007).

Acknowledgments: We acknowledge the PVA samples provided by Kuraray. J.L. acknowledges the GE Graduate Fellowship for Innovation and the FEI Fellowship. S.Z. acknowledges the GE Graduate Fellowship for Innovation. The SAXS instrument was acquired through an NSF grant (MRI-1228817). We thank M. T. Shaw for many valuable discussions. **Funding:** This research was sponsored by the NSF (CMMI-1562907). Additionally, Y.X. was partially supported by the National Science Foundation (CBET 1510468). **Author contributions:** L.S. conceived the idea. F.D. and J.L. prepared the samples and optimized the preparation steps. F.D., J.L., S.Z., and K.M.W. conducted most of the characterizations. Y.X. and M.-P.N. performed the SAXS characterization and the corresponding analysis. F.D., J.L., and L.S. wrote the first draft of the manuscript. All authors contributed to revise the manuscript. **Competing interests:** L.S. and F.D. are authors on a patent application related to this work, which was filed on 18 October 2012 and published on 24 April 2014 (WO 2014/063009). The other authors declare that they have no competing interests. **Data and materials availability:** All data needed to evaluate the conclusions in the paper are present in the paper and/or the Supplementary Materials. Additional data related to this paper may be requested from the authors.

Submitted 17 April 2017
Accepted 15 June 2017
Published 19 July 2017
10.1126/sciadv.1701212

Citation: F. Ding, J. Liu, S. Zeng, Y. Xia, K. M. Wells, M.-P. Nieh, L. Sun, Biomimetic nanocoatings with exceptional mechanical, barrier, and flame-retardant properties from large-scale one-step coassembly. *Sci. Adv.* **3**, e1701212 (2017).